Strong texturing of lithium metal in batteries

Feifei Shi[a], Allen Pei[a], Arturas Vailionis[b], Jin Xie[a], Bofei Liu[a], Jie Zhao[a], Yongji Gong[a], and Yi Cui[a,c,1]

[a]Department of Materials Science and Engineering, Stanford University, Stanford, CA 94305; [b]Stanford Nano Shared Facilities, Stanford University, Stanford, CA 94305; and [c]Stanford Institute for Materials and Energy Sciences, Stanford Linear Accelerator Center National Accelerator Laboratory, Menlo Park, CA 94025

Edited by Thomas E. Mallouk, The Pennsylvania State University, University Park, PA, and approved October 6, 2017 (received for review May 17, 2017)

Lithium, with its high theoretical specific capacity and lowest electrochemical potential, has been recognized as the ultimate negative electrode material for next-generation lithium-based high-energy-density batteries. However, a key challenge that has yet to be overcome is the inferior reversibility of Li plating and stripping, typically thought to be related to the uncontrollable morphology evolution of the Li anode during cycling. Here we show that Li-metal texturing (preferential crystallographic orientation) occurs during electrochemical deposition, which governs the morphological change of the Li anode. X-ray diffraction pole-figure analysis demonstrates that the texture of Li deposits is primarily dependent on the type of additive or cross-over molecule from the cathode side. With adsorbed additives, like $LiNO_3$ and polysulfide, the lithium deposits are strongly textured, with Li (110) planes parallel to the substrate, and thus exhibit uniform, rounded morphology. A growth diagram of lithium deposits is given to connect various texture and morphology scenarios for different battery electrolytes. This understanding of lithium electrocrystallization from the crystallographic point of view provides significant insight for future lithium anode materials design in high-energy-density batteries.

lithium metal | texture | battery | electrocrystallization | morphology

The emerging demand for electric vehicles has stimulated the development of high-energy storage systems, especially the lithium–sulfur and lithium–air batteries that employ lithium metal anodes (1–4). Lithium (Li), with its extremely high theoretical specific capacity (3,860 mAh g^{-1}) and lowest electrochemical potential (−3.04 V vs. SHE), has since been recognized as an ultimate negative electrode material. There has been research over the past four decades on Li metal (5–9). Recently there has been a renaissance of Li-metal anode research, particularly through a wide variety of materials, interface, and electrolyte design (10–15). However, the industrial deployment of Li-metal batteries has still been postponed by its poor cycling efficiency and safety, both of which stem from the uncontrollable Li deposition process. While various theories for understanding lithium electrodeposition have been given in the past, the mechanisms underlying lithium growth are still hotly debated (8). Compared with normal metal deposition, lithium deposition in batteries is a more complex electrocrystallization process. The adsorption of aprotic solvent molecules, paired anions, and additives on the as-deposited Li affects interface energetics; in addition, the electrolyte-specific solid electrolyte interphase (SEI) layer further complicates the process. While it has been recently reported that the morphology of lithium deposits is related to the electrolyte and formed SEI layer, there is a lack of fundamental understanding of the mechanism behind the correlation (16–18).

The various characteristic morphologies of lithium deposits grown in different electrolyte systems have been identified and discussed (16, 19). The shape of metal crystals is commonly controlled by and strongly dependent on their crystallographic nature (20). Inspired by observations of how electrolyte identity and composition affect Li deposit morphology (7, 21–25), we are interested in taking a further step to understand if their crystallographic growth habits drive the Li morphological evolution. After all, the electrodeposition of Li is a crystallization process, and it is worthwhile to correlate its phenomenological morphology to its crystallization nature. Typically, due to the adsorption of additives onto active growth sites, electrodeposition processes promote preferential growth of particular grain orientations, inducing an anisotropic crystal orientation distribution known as "texture" (26) and consequently leading to certain grain morphologies. Such an additive adsorption effect is expected for the case of lithium electrodeposition. However, the high reactivity and poor X-ray scattering resulting from the low atomic number of Li bring a great deal of difficulty for traditional crystallographic characterization (27–29), which makes the area of texture study of lithium metal an almost blank space. Thus, it is highly demanding to explore novel characterization and analysis methods for lithium battery electrode application (30, 31).

This study mainly focuses on characterizing the anisotropic orientation distribution of crystallographic grains in electrodeposited lithium films under various electrolyte environments and understanding how the crystallographic texture is related to common morphologies. X-ray diffraction and pole-figure analysis are used as tools to probe the crystallographic orientation distribution of electrodeposited lithium films. Here, both carbonate and ether-based electrolyte systems have been tested with and without additives. Lithium anodes from Li–S and Li–O_2 full-cell batteries have also been investigated. We find that the texture of Li deposits significantly depends on the additives and any cathode cross-over molecules present in the electrolyte, which intrinsically leads to varied morphology. For example, with the adsorption of strong inhibitors like lithium polysulfides and lithium nitrate ($LiNO_3$), the crystallographic grains of lithium deposits prefer to align with Li (110) planes parallel to the substrate and form uniform round-shaped deposits. We use exchange current density as an indicator to correlate the electrolyte additive type with texture, and explore

Significance

This work represents a first attempt to study the crystallographic texture of Li metal in batteries. X-ray diffraction pole-figure analysis demonstrates that the texture of Li deposition is primarily dependent on the type of additive or cross-over molecule from the cathode side. We find that reversibility of Li, which is phenomenologically influenced by morphology, is fundamentally driven by the texture (crystallographic orientation). Additives in electrolytes and the cross-over molecules from the cathode play crucial roles on the crystallographic texture because they hinder the cathodic process and selectively adsorb/react on different crystal planes. Additives with favorable adsorption and reusability will generate controllable texture, resulting in more uniform morphology and better cycling reversibility.

Author contributions: F.S. and Y.C. designed research; F.S., A.P., A.V., J.X., B.L., J.Z., and Y.G. performed research; and F.S., A.P., and Y.C. wrote the paper.

The authors declare no conflict of interest.

This article is a PNAS Direct Submission.

[1]To whom correspondence should be addressed. Email: yicui@stanford.edu.

This article contains supporting information online at www.pnas.org/lookup/suppl/doi:10.1073/pnas.1708224114/-/DCSupplemental.

its effect in various electrolyte systems. The present work provides further fundamental understanding of lithium electrocrystallization, which will be a vital route to rationalize the use of additives in Li battery electrolytes.

Result and Discussion

Lithium Deposit Morphology. Different characteristic morphology types for Li-metal deposits have been reported in previous studies on individual electrolyte systems (16, 22, 23). Here we compared the morphologies of lithium deposition in various electrolyte systems at a low current density of 0.1 mA/cm^2. To eliminate the crimping pressure and separator effect, we used a "lift-up" coin cell setup for all of the lithium deposition in this work (32, 33). More details are given in *SI Appendix* and *SI Appendix*, Fig. S1. As shown in Fig. 1*A*, whisker-shaped elongated lithium deposits are formed in a typical carbonate-based electrolyte, ethylene carbonate/diethyl carbonate (EC/DEC, 1:1 vol/vol), 1 M $LiPF_6$. Carbonate-based solvents are commonly used in batteries due to their large electrochemical decomposition window, enabling the coupling of Li metal with high-voltage cathodes (34). To investigate the effects of other current densities on Li deposits, we deposited lithium at current densities ranging from 0.1 to 5 mA/cm^2 (*SI Appendix*, Fig. S3). Within this current range, while the size of Li deposits decreases with increasing current density, the characteristic shape of deposits does not change, suggesting that within normal operational range, current density plays a less-pronounced role on the Li morphology. Fig. 1*B* shows lithium deposited in 1,3-dioxolane/1,2-dimethoxyethane (DOL/DME, 1:1 vol/vol), 1 M LiTFSI, 1% $LiNO_3$, which has a characteristic rounded shape (35). Similar current-density effects on the size and morphology of Li deposits in this electrolyte have also observed (35). Lithium deposits (Fig. 1*C*) are round-shaped when the electroplating process is done in a Li–S full battery with 5 M poly-sulfide as catholyte. We found that with the addition of polysulfide in DOL/DME with 1% $LiNO_3$, lithium deposits are uniform and round-shaped, even at higher current density and on the edge of the current collector. This is consistent with previous reports that polysulfide and lithium nitrate will have synergetic effects to prevent the growth of whisker-shaped deposits (22). Li deposition in a Li–O_2 full battery with ether-based electrolytes also exhibits round particle morphologies (Fig. 1*D*), which validates that dendrite formation has not been observed in Li–O_2 cells tested to date (3). It is commonly reported that ether-based electrolytes generate elastic SEI films, eliminating the whisker-shaped deposits (36, 37). However, control Li deposition experiments using DOL/DME and tetraethylene glycol dimethyl ether (TEGDME), ether-based electrolytes, alone with no additives, still resulted in whisker-shaped deposits (*SI Appendix*, Figs. S4 and S5). After screening different types of battery electrolytes, we systematically observed that beyond the current density and electrolyte solvent identity, the specific additives (e.g., $LiNO_3$) or the cross-over molecules (O_2, polysulfide) from the cathode side play a major role in the morphology of Li deposits.

Texture Analysis of Li Deposits Using X-Ray Pole Figures. It has been known that the diverse growth conditions of the metallic films strongly affect grain sizes and their crystallographic orientations. During film growth, the crystalline grains undergo nucleation, growth, coarsening, coalescence, and thickening (38). All these stages of growth affect the final microstructural properties of the polycrystalline film. Here we examine the crystallographic orientation distribution of electrocrystallized Li in the presence of different electrolytes and additives. X-ray diffraction is known to be a standard method for determining the crystallographic structure, atomic arrangement, as well as grain orientation in a variety of materials. Usually, a conventional symmetric θ-2θ scan, as shown in Fig. 2*A*, is performed to learn about the metal film microstructure. In this case, however, only the grains with lattice planes that are oriented parallel or nearly parallel to the thin-film surface are detected. Fig. 2*B* shows typical X-ray diffraction data obtained from Li-metal foil using a symmetric θ-2θ scan (*Top*) as well as data from the powder-diffraction file for Li powder (*Bottom*). A comparison between measured Bragg peak intensities and those published in powder-diffraction files from randomly oriented powder usually provides ambiguous results of crystallographic grain orientation distribution due to the large grain sizes in Li foil, resulting in poor statistics. The complete crystallographic orientation distribution can be obtained by collecting so-called pole figures of different (*hkl*) planes and analyzing

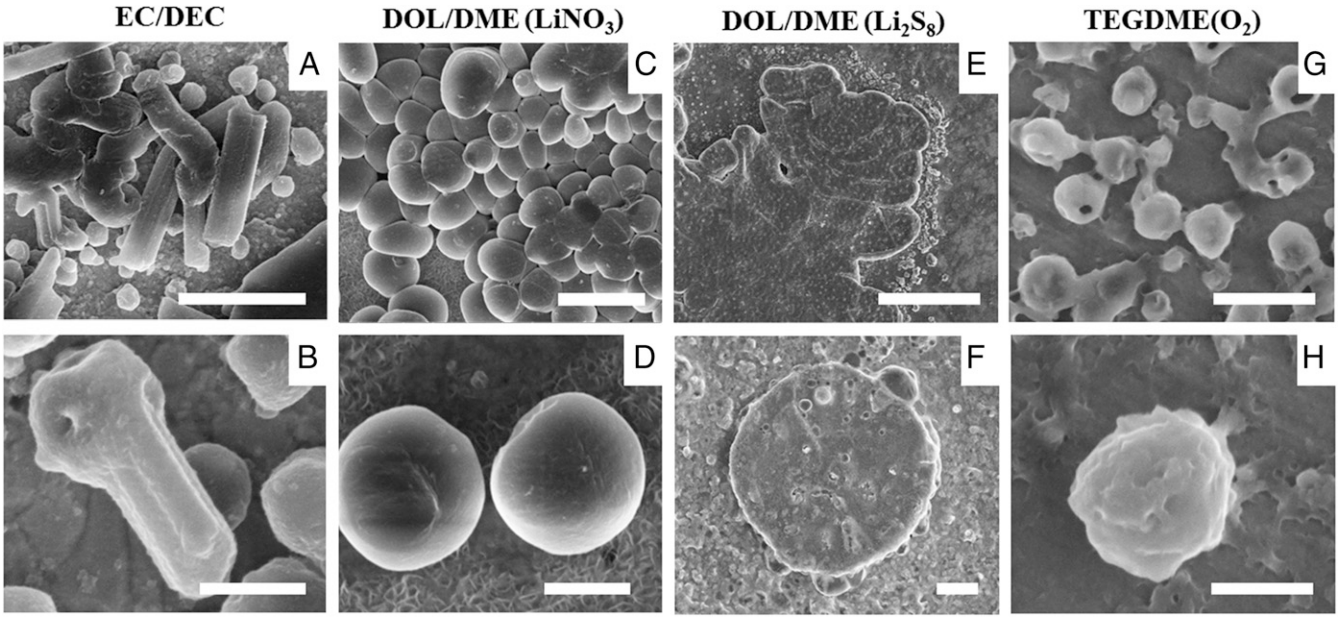

Fig. 1. Lithium deposition morphology in various electrolyte systems at the current density of 0.1 mA/cm^2, 1 mAh/cm^2. (*A* and *B*) EC/DEC 1 M $LiPF_6$. (*C* and *D*) DOL/DME 1 M LiTFSI, 1% $LiNO_3$. (*E* and *F*) Sulfur catholyte 5 M S_8 dissolved in DOL/DME 1 M LiTFSI, 1% $LiNO_3$. (*G* and *H*) TEGDME 1 M LiTFSI with Li_2O_2 as cathode. (Scale bars: *A*, *C*, and *G*, 5 μm; *E*, 20 μm; *D* and *F*, 2 μm; *B* and *H*, 1 μm.)

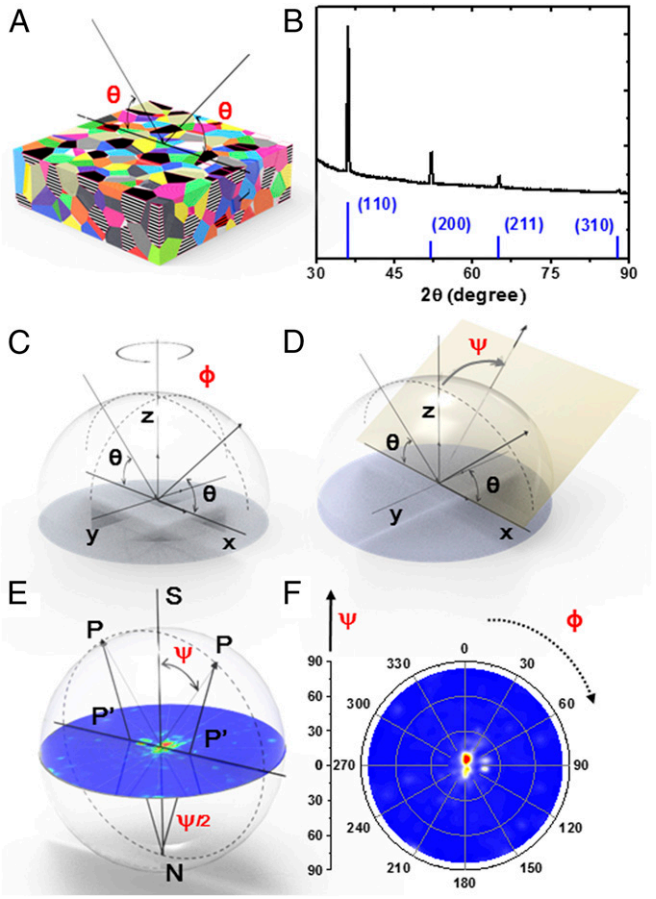

Fig. 2. Schematic representation of pole-figure measurement (*A*) symmetric θ-2θ scan, (*B*) X-ray diffraction data of lithium metal and the data from powder-diffraction file of lithium, (*C*) the angle of rotation ϕ that measures the azimuth of the sample in the surface plane, (*D*) the tilt angle ψ that defines the amount of tilting of the sample with respect to the normal to the sample surface, (*E*) stereographic projection of Bragg reflection intensity distribution, and (*F*) Li (200) pole figure of commercial Li foil.

their orientation with respect to the sample coordination frame. The pole figures are usually collected by varying the angle of rotation ϕ that measures the azimuth of the sample in the surface plane and the tilt angle ψ that defines the amount of tilting of the sample with respect to the normal to the sample surface, as shown in Fig. 2 *C* and *D*. ϕ and ψ are varied from 0–360° and 0–90°, respectively. Thus, the intensity of a particular Bragg reflection measured under varying sample orientations yields an intensity distribution I(*hkl*) as a function of the ϕ and ψ angles over a 3D sphere which defines the crystallographic orientation distribution of grains in the film. As shown in Fig. 2*E*, this intensity distribution is represented as a stereographic projection where intensity points, $P = I(\phi, \psi)$, from a 3D sphere are projected onto a plane as $P' = I(\phi, \psi)$. This way, the pole figure represents a variation of the pole density and pole orientation for a selected set of crystallographic planes. Fig. 2*F* illustrates a typical Li(200) pole figure of a commercial Li foil with its intensity mainly located at the origin. The polycrystalline metal films might develop complex textures with considerable orientation spreads; therefore, the interpretation of a single pole figure in terms of specific grain orientations is difficult and frequently ambiguous. To understand the texture of the material, it is necessary to collect and analyze two or more pole figures of different (*hkl*) reflections. In this work, due to the in-plane isotropy of electrodeposited lithium film, we mainly focus on the texture along out-of-plane directions in the following discussion.

Fig. 2*B* shows data from a symmetric θ-2θ scan where Li (110) and Li (200) peaks can be resolved as the two major diffraction peaks. The scan is compared with the Li powder-diffraction file representing randomly oriented Li grains. Two pole figures were collected for Li-metal film at 2θ angles of 36.19° and 51.97° corresponding to the locations of (110) and (200) Bragg peaks, respectively. The beam spot size was chosen to be 1 cm × 1 cm. We chose this size to make it large enough to include a sufficient number of grains with sizes ranging from 10 to 100 μm. In Fig. 3*A*, the pole figures for plain lithium metal foil show a typical texture for deformed metals. Commercial lithium foils, which have a typical silver metallic color with grain sizes of around 100 μm, are formed by rolling compression. The Li(200) pole figure shows that almost all of the intensity is located at the center, where tilt angle ψ is equal to zero. This indicates that the rolled sheets of lithium have [100] out-of-plane preferred orientation (39). The nature of the deformation texture depends essentially on the crystal structure of the metal and the extent of plastic flow. Lithium is a body-centered-cubic (bcc) metal, and thus its sheet texture is very similar to other bcc metals (40). The (110) and (200) pole figures for Li electrodeposits in various electrolyte environments are given in Fig. 3 *B*–*D*. The left column shows SEM characterizations of their surface morphology. The deposits in EC/DEC electrolyte are whisker-shaped and randomly aligned, and accumulate randomly during the electroplating process. The representative (110) pole figure shows a disk-shaped, radially uniform diffraction intensity distribution, which indicates that the film's texture is not clearly pronounced. The (200) pole figure of the same sample shows a broad ring at an angle around ψ = 45° equal to the angle between (110) and (100) planes. Even though each whisker is a single crystallite, the almost random orientations of whiskers result in a rather broad distribution of crystallographic grain orientations and increase the roughness of the deposited Li film. As previously discussed, at the current density of 0.1 mA cm^{-2} in DOL/DME electrolytes with only $LiNO_3$ and DOL/DME with both $LiNO_3$ and polysulfide additives, the morphological shape of lithium deposits is round. It has been reported that the addition of polysulfides can further suppress the formation of whisker-shaped deposits on the edge of the current collector at the current density of 2 mA cm^{-2} (22). Fig. 3 *C* and *D* shows (110) pole figures that exhibit a sharp intensity concentration around ψ = 0°, indicating that the round-shaped Li deposits are mostly textured with (110) planes parallel to the electrode substrate. Additionally, as can be seen from the intensity at the origin of the (200) pole figure in Fig. 3*C*, the Li deposit in DOL/DME with $LiNO_3$ contains a small portion of [100] out-of-plane–oriented crystallites, which may be due to the nonuniform deposition on the edge of current collector (22). While the Li (100) plane has the lowest surface energy versus vacuum (41), the more pronounced [110] texture could be a result of strong adsorption of the $LiNO_3$ and polysulfide additives during the crystal growth. To elucidate the origin of texture in electrochemically deposited lithium, we discuss current density, SEI layers, and inhibitor factors in various electrolytes in the following section.

Factors Influencing Lithium Deposits.

Current density. Current density is one of the most important parameters discussed for lithium deposition (19). When the diffusion-limiting current $J_{limiting}$ is exceeded, the rate of Li^+ consumption by deposition exceeds the rate at which Li^+ can be replenished by diffusion. After Sand's time, the ionic concentration at the working electrode drops to zero. This complete concentration polarization will cause the ramification of the electroplated species. Thus, we calculated the diffusion-limiting current density for EC/DEC and DOL/DME electrolytes and the ratio of commonly used current densities to the diffusion-limiting current density for typical batteries

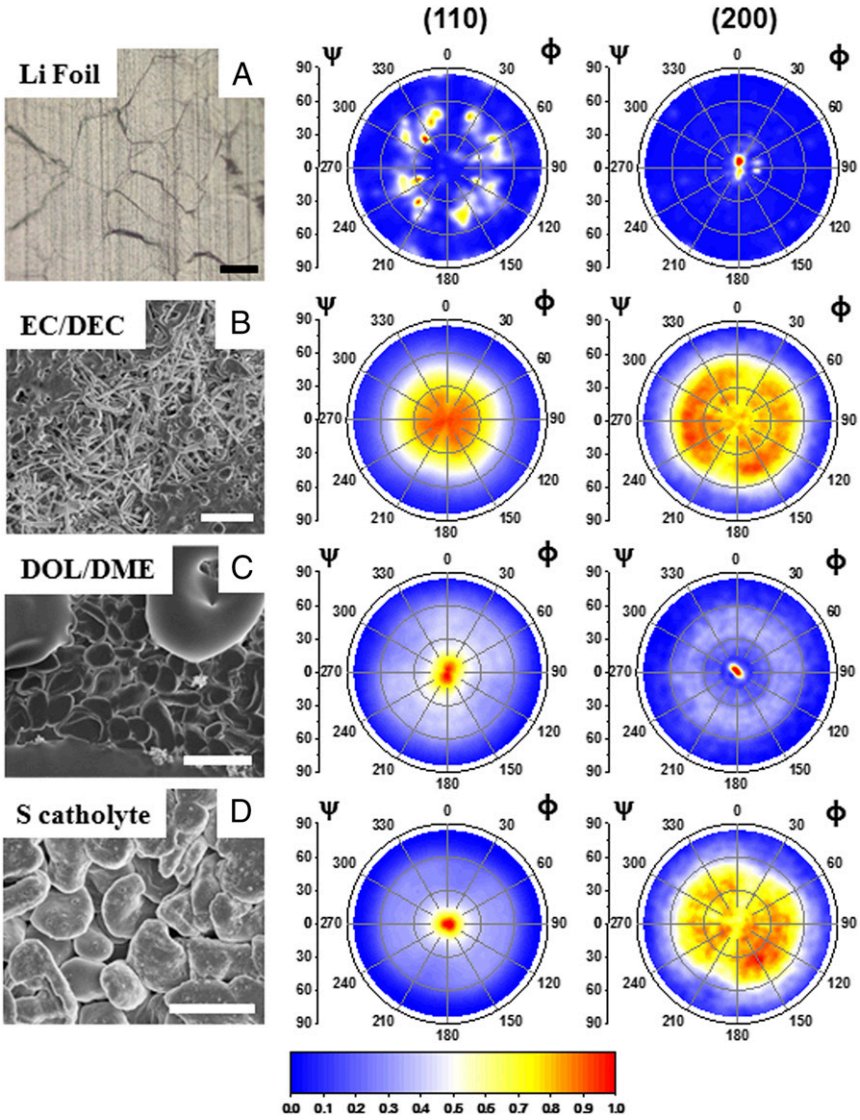

Fig. 3. Pole-figure analysis of Li films. (*A*) Li foil; (*B*) Li deposit in EC/DEC 1 M $LiPF_6$; (*C*) Li deposit in DOL/DME 1 M LiTFSI, 1% $LiNO_3$; and (*D*) Li deposit in sulfur catholyte 5 M S_8 dissolved in DOL/DME 1 M LiTFSI, 1% $LiNO_3$. All of the absorbance intensities are normalized to its largest value. (Scale bar: 20 μm.)

(*SI Appendix*, Table S1). We found that in coin cells, normal operational current densities are around two orders of magnitude smaller than the diffusion-limiting current density (152 mA/cm^2 for EC/DEC, 198 mA/cm^2 for DOL/DME), indicating the $J_{limiting}$ is rarely reached. *SI Appendix*, Figs. S3–S5 show that the shapes of lithium deposits in electrolytes without additives do not change, despite the diameter of deposits decreasing with increasing current density (tested from 0.1 to 5 mA/cm^2). Smaller current density will generate a larger size of lithium deposits, thus reducing the surface-area/SEI consumption and improve cycling efficiency (35). However, this approach is not always practical in real Li-metal batteries, due to the limitation of charging rate.

SEI layer. The SEI layer has been recognized as a unique and critical factor during lithium-metal deposition. A "good" passivation layer needs to be elastic, flexible, chemically stable, and accommodate the volume changes of the anode during its electrochemical processes. Here we carried out both X-ray photoelectron spectroscopy and IR spectroscopy analysis to characterize the chemical compositions of the SEI in various electrolyte. SEI formed in carbonate electrolytes mainly consist of alkyl carbonate-based components, as seen from -CO_3 functional groups in *SI Appendix*, Figs. S6*A* and S7*A*. The SEI layers formed in ether-based electrolytes are reported to be ether oligomers, consisting of -CO and -COOR functional groups in *SI Appendix*, Figs. S6 *B–E* and S7 *B–E*. Interestingly, there is no obvious morphology change among carbonate and ether electrolyte without additives, although the elastomeric SEI formed in ether systems are reported to suppress lithium dendrite growth (36, 37). With the addition of $LiNO_3$, the organic components are similar, except the $LiNO_2$ species show up. With the addition of both $LiNO_3$ and polysulfide, the main new component is Li_2S/Li_2S_2. Ultimately, even though differences in SEI composition in different electrolyte systems are clear, it is still hard to correlate the morphology and texture of lithium deposits with their SEI layer.

Inhibitors. Inhibitors are the species physically or chemically adsorbed on the surface of the electrode, in the double layer, or in the diffusion layer (42). They hinder the cathodic process and are thus called inhibitors. In the electroplating industry, inhibitor additives are widely applied to generate compact and smooth metal coatings. However, for the Li-metal system, the rapidly absorbed additives and electrolyte solvents are believed to be subsequently reduced and become incorporated into the SEI layer on lithium due to its low potential. To differentiate between the role of the

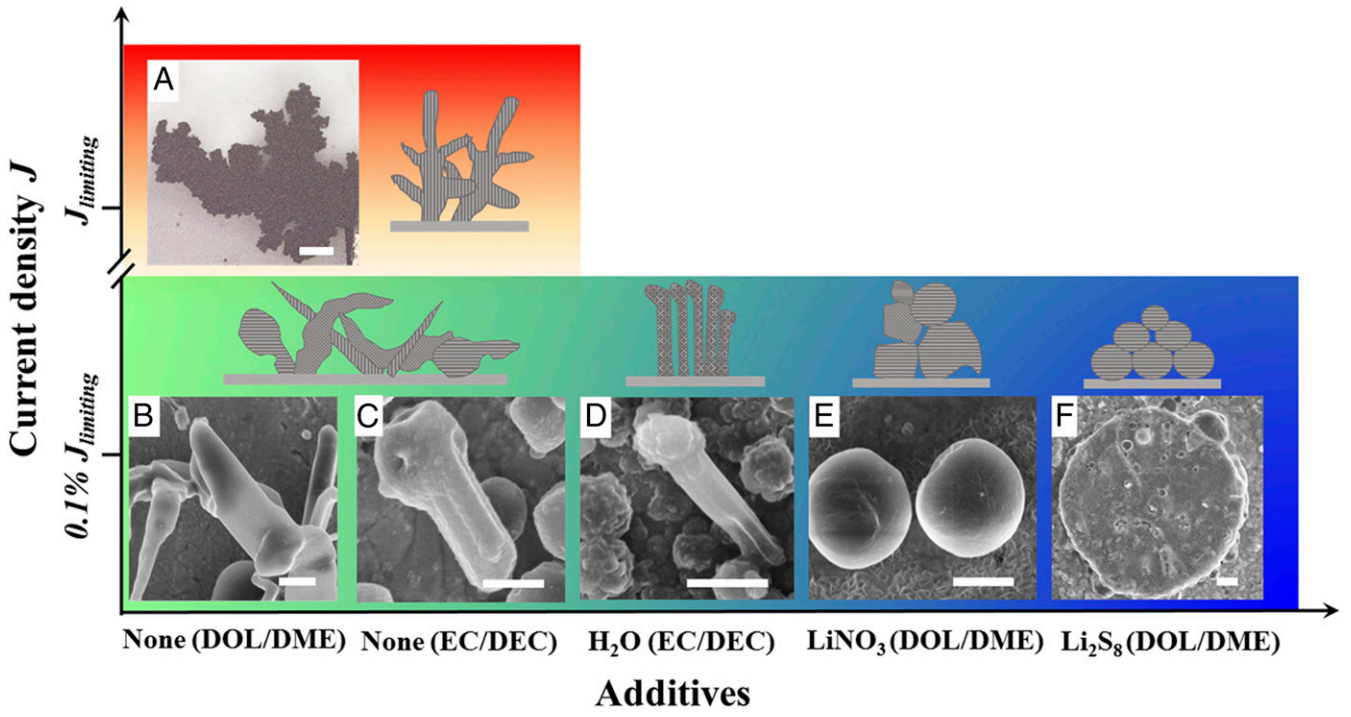

Fig. 4. Growth of lithium electrodeposits as a function of current density J and additives in electrolyte. Characteristic images of Li deposits (with schematics on the right-hand side or above) are plotted based on the current density and additive type, with inhibition intensity increasing in the horizontal direction. (*A*) Exceeding diffusion-limited current density $J_{limiting}$, optical image of dendritic and ramified Li deposit in EC/DEC 1 M $LiPF_6$, below 0.1% of diffusion-limited current density $J_{limiting}$. SEM images of lithium deposit in (*B*) DOL/DME 1 M LiTFSI; (*C*) EC/DEC 1 M $LiPF_6$; (*D*) EC/DEC 1 M $LiPF_6$, 100 ppm H_2O; (*E*) DOL/DME 1 M LiTFSI, 1% $LiNO_3$; and (*F*) sulfur catholyte, 5 M S_8 dissolved in DOL/DME 1 M LiTFSI, 1% $LiNO_3$. (Scale bar: *A*, 200 μm; *B*, *E*, and *F*, 2 μm; *C* and *D*, 1 μm.)

adsorption of electrolytes/additives and the influence of the SEI layer during the deposition of lithium, we measured the exchange current density of the Li/Li^+ couple using microelectrodes and performed impedance spectroscopy on lithium electrodes in various electrolytes (*SI Appendix*, Figs. S5 and S6 and Table S2). The exchange current density (j_0) describes the rate of electron transfer that occurs at zero overpotential, and it is widely understood to be a measure of the inhibition intensity in classical systems (42). Microelectrodes prevent mass-transfer-related limitations in high rate processes, and are thus useful for studying fast, film-free Li deposition before the SEI film formation process occurs (43). Lower values of j_0 indicate a higher tendency to adsorb inhibitors in the electrolyte (inhibited Faradaic charge transfer) and vice versa.

For carbonate-based electrolytes, the plain EC/DEC electrolyte with no additives showed the highest exchange current density of 35 mA/cm^2. Upon the addition of inhibiting additives, the measured exchange current density decreased to 28 mA/cm^2 for 100 ppm water. This decrease in j_0 can be attributed to the inhibiting effect of the resulting HF molecules, which cause Li to grow as well-aligned crystal rods (44). A similar trend of decreasing j_0 with increasing inhibition was observed for ether-based electrolytes. The measured exchange current density for plain DOL/DME electrolyte with no additives was 123 mA/cm^2, which decreased to 27 mA/cm^2 with the addition of 1% wt. $LiNO_3$. With the addition of both 1% wt. $LiNO_3$ and 1 μM Li_2S_8 as additives, the exchange current density further decreased to 25 mA/cm^2. The morphology of lithium deposits in ether electrolyte transitions from randomly oriented whiskers (*SI Appendix*, Fig. S4) to compactly packed round disks as the exchange current density decreases. Thus, the adsorption of inhibitor molecules in the electrolyte is the dominant factor that leads to texturing of electrochemically deposited lithium.

Fig. 4 shows a growth diagram of lithium, summarizing the effects of commonly used additives and current density on lithium morphology. Here, schematic diagrams and characteristic SEM images of Li deposits are plotted based on the current density used and additives used, with inhibition intensity increasing in the horizontal direction. Li grown at overlimiting current densities is ramified and dendritic, as commonly seen in cells with large electrode spacings (19) (Fig. 4*A*). Due to the inhomogeneity of the SEI layer, the local current density of lithium deposition could be large even though the apparent current density is small, leading to the dendritic growth initiation below limiting current density. For current densities that are far below the limit (0.1% $J_{limiting}$), in the case of none/weak inhibition (EC/DEC and DOL/DME electrolyte without any additives), the deposits usually show a whisker-like shape (Fig. 4 *B* and *C*). This morphology is consistent with recent works where lithium is electrodeposited in high-vacuum conditions and with polyethylene oxide solid polymer electrolytes where there are no inhibitors present in the form of electrolyte solvent or additives (45, 46). As the inhibition intensity increases, basis-oriented reproduction-type deposits are observed and are characterized by a large number of elongated crystals perpendicular to the substrate, forming a coherent deposit (42) (Fig. 4*D*). This lithium texture has been reported with the addition of HF and $CsPF_6$ as additives (25, 47). With strong inhibitors, such as $LiNO_3$ or polysulfides, field-oriented texture-type deposits emerge (Fig. 4 *E* and *F*). Strong texturing generates compact lithium deposits, thus reducing the surface area and resulting in less SEI formation, electrolyte consumption, and dead lithium, which consequently improves cycling efficiency.

Conclusion

We found the crystallographic texture of electrocrystallized lithium films in lithium batteries using X-ray diffraction and pole-figure analysis. The pole figures demonstrate that the morphology of the electrodeposited lithium film is intrinsically determined by

crystallographic texture. Strongly textured lithium typically corresponds to compact, well-aligned lithium deposits, while weak/non-textured lithium has mossy and whisker-like structure. Compared with the effect of the current density, additives in electrolytes and the cross-over molecules from the cathode play a critical role in the crystallographic texture because they hinder the cathodic process and selectively adsorb on different crystal planes. A Li deposit growth diagram is constructed to connect the gap between electrolyte and morphology of lithium deposits. The electrolytes with additives of lower exchange current density will generate stronger texture, thus more uniform morphology. Designing new types of additives with high inhibition capability leading to controllable texture will be one of the most promising paths to better lithium metal batteries.

Materials and Methods

Materials and methods can be found in *SI Appendix*.

ACKNOWLEDGMENTS. The work was supported by the Assistant Secretary for Energy Efficiency and Renewable Energy, Office of Vehicle Technologies of the US Department of Energy under the Battery 500 Consortium program. A.P. acknowledges support by the Department of Defense through the National Defense Science & Engineering Graduate Fellowship Program and support by the Stanford Graduate Fellowship. Part of this work was performed at the Stanford Nano Shared Facilities (SNSF), supported by the National Science Foundation under Award ECCS-1542152.

1. Bruce PG, Freunberger SA, Hardwick LJ, Tarascon J-M (2011) Li-O_2 and Li-S batteries with high energy storage. *Nat Mater* 11:19–29.
2. Sun Y, Liu N, Cui Y (2016) Promises and challenges of nanomaterials for lithium-based rechargeable batteries. *Nat Energy* 1:16071.
3. Lu J, et al. (2014) Aprotic and aqueous Li-O_2 batteries. *Chem Rev* 114:5611–5640.
4. Peng Z, Freunberger SA, Chen Y, Bruce PG (2012) A reversible and higher-rate Li-O_2 battery. *Science* 337:563–566.
5. Fraioly AV, Barber WA, Feldman AM (1970) US Patent 3,551,205.
6. Selim R, Bro P (1974) Some observations on rechargeable lithium electrodes in a propylene carbonate electrolyte. *J Electrochem Soc* 121:1457–1459.
7. Aurbach D, et al. (2002) Attempts to improve the behavior of Li electrodes in rechargeable lithium batteries. *J Electrochem Soc* 149:A1267–A1277.
8. Xu W, et al. (2014) Lithium metal anodes for rechargeable batteries. *Energy Environ Sci* 7:513–537.
9. Aurbach D, Zinigrad E, Teller H, Dan P (2000) Factors which limit the cycle life of rechargeable lithium (metal) batteries. *J Electrochem Soc* 147:1274–1279.
10. Lin D, et al. (2016) Layered reduced graphene oxide with nanoscale interlayer gaps as a stable host for lithium metal anodes. *Nat Nanotechnol* 11:626–632.
11. Yan K, et al. (2016) Selective deposition and stable encapsulation of lithium through heterogeneous seeded growth. *Nat Energy* 1:16010.
12. Zheng G, et al. (2014) Interconnected hollow carbon nanospheres for stable lithium metal anodes. *Nat Nanotechnol* 9:618–623.
13. Zinigrad E, et al. (2004) Investigation of lithium electrodeposits formed in practical rechargeable Li-Li$_x$$MnO_2$ batteries based on LiAsF_6/1,3-dioxolane solutions. *J Electrochem Soc* 151:A111–A118.
14. Lin D, Liu Y, Cui Y (2017) Reviving the lithium metal anode for high-energy batteries. *Nat Nanotechnol* 12:194–206.
15. Mikhaylik Y, et al. (2010) High energy rechargeable Li-S cells for EV application. Status, remaining problems and solutions. *ECS Trans* 25:23–34.
16. Zhang J-G, Xu W, Henderson WA (2016) *Lithium Metal Anodes and Rechargeable Lithium Metal Batteries* (Springer, Cham, Switzerland), pp 6–14.
17. Steiger J, Richter G, Wenk M, Kramer D, Mönig R (2015) Comparison of the growth of lithium filaments and dendrites under different conditions. *Electrochem Commun* 50: 11–14.
18. Steiger J, Kramer D, Mönig R (2014) Mechanisms of dendritic growth investigated by in situ light microscopy during electrodeposition and dissolution of lithium. *J Power Sources* 261:112–119.
19. Bai P, Li J, Brushett FR, Bazant MZ (2016) Transition of lithium growth mechanisms in liquid electrolytes. *Energy Environ Sci* 9:3221–3229.
20. Xia Y, Xiong Y, Lim B, Skrabalak SE (2009) Shape-controlled synthesis of metal nanocrystals: Simple chemistry meets complex physics? *Angew Chem Int Ed Engl* 48: 60–103.
21. Lu Y, Tu Z, Archer LA (2014) Stable lithium electrodeposition in liquid and nanoporous solid electrolytes. *Nat Mater* 13:961–969.
22. Li W, et al. (2015) The synergetic effect of lithium polysulfide and lithium nitrate to prevent lithium dendrite growth. *Nat Commun* 6:7436.
23. Qian J, et al. (2015) High rate and stable cycling of lithium metal anode. *Nat Commun* 6:6362.
24. Besenhard JO, Gurtler J, Komenda P, Paxinos A (1987) Corrosion protection of secondary lithium electrodes in organic electrolytes. *J Power Sources* 20:253–258.
25. Zhang Y, et al. (2014) Dendrite-free lithium deposition with self-aligned nanorod structure. *Nano Lett* 14:6889–6896.
26. Kocks UF, Tome CN, Wenk H-R (1998) *Texture and Anisotropy: Preferred Orientations in Polycrystals and Their Effect on Materials Properties* (Cambridge Univ Press, Cambridge, UK), pp 44–94.
27. Huang JY, et al. (2010) In situ observation of the electrochemical lithiation of a single SnO_2 nanowire electrode. *Science* 330:1515–1520.
28. Matsui M (2011) Study on electrochemically deposited Mg metal. *J Power Sources* 196: 7048–7055.
29. Gireaud L, Grugeon S, Laruelle S, Yrieix B, Tarascon J-M (2006) Lithium metal stripping/plating mechanisms studies: A metallurgical approach. *Electrochem Commun* 8: 1639–1649.
30. Ulvestad A, et al. (2015) BATTERIES. Topological defect dynamics in operando battery nanoparticles. *Science* 348:1344–1347.
31. Ebner M, Marone F, Stampanoni M, Wood V (2013) Visualization and quantification of electrochemical and mechanical degradation in Li ion batteries. *Science* 342: 716–720.
32. Ryou M-H, Lee YM, Park J-K, Choi JW (2011) Mussel-inspired polydopamine-treated polyethylene separators for high-power Li-ion batteries. *Adv Mater* 23:3066–3070.
33. Jana A, Ely DR, García RE (2015) Dendrite-separator interactions in lithium-based batteries. *J Power Sources* 275:912–921.
34. Xu K (2014) Electrolytes and interphases in Li-ion batteries and beyond. *Chem Rev* 114:11503–11618.
35. Pei A, Zheng G, Shi F, Li Y, Cui Y (2017) Nanoscale nucleation and growth of electrodeposited lithium metal. *Nano Lett* 17:1132–1139.
36. Yamaki J-i, et al. (1998) A consideration of the morphology of electrochemically deposited lithium in an organic electrolyte. *J Power Sources* 74:219–227.
37. Aurbach D (2000) Review of selected electrode–solution interactions which determine the performance of Li and Li ion batteries. *J Power Sources* 89:206–218.
38. Thompson CV (2000) Structure evolution during processing of polycrystalline films. *Annu Rev Mater Sci* 30:159–190.
39. Brodusch N, Zaghib K, Gauvin R (2015) Electron backscatter diffraction applied to lithium sheets prepared by broad ion beam milling. *Microsc Res Tech* 78:30–39.
40. Hu H (1974) Texture of metals. *Texture* 1:233–258.
41. Yoo S-H, Lee J-H, Jung Y-K, Soon A (2016) Exploring stereographic surface energy maps of cubic metals via an effective pair-potential approach. *Phys Rev B* 93:035434.
42. Winand R (1992) Electrocrystallization-theory and applications. *Hydrometallurgy* 29: 567–598.
43. Aurbach D (1999) *Nonaqueous Electrochemistry* (Marcel Dekker, New York), pp 336–345.
44. Qian J, et al. (2015) Dendrite-free Li deposition using trace-amounts of water as an electrolyte additive. *Nano Energy* 15:135–144.
45. Tang C-Y, Dillon SJ (2016) In situ scanning electron microscopy characterization of the mechanism for Li dendrite growth. *J Electrochem Soc* 163:A1660–A1665.
46. Dolle M, Sannier L, Beaudoin B, Trentin M, Tarascon J-M (2002) Live scanning electron microscope observations of dendritic growth in lithium/polymer cells. *Electrochem Solid-State Lett* 5:A286–A289.
47. Shiraishi S, Kanamura K, Takehara Z-i (1997) Study of the surface composition of highly smooth lithium deposited in various carbonate electrolytes containing HF. *Langmuir* 13:3542–3549.